

Late First-Row Transition Metal Complexes of a Tetradentate Pyridinophane Ligand: Electronic Properties and Reactivity Implications

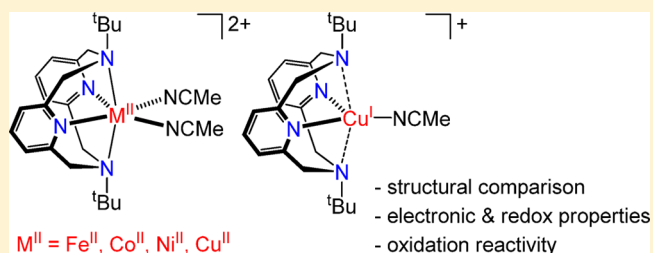
Julia R. Khusnutdinova,[†] Jia Luo,[†] Nigam P. Rath,[‡] and Liviu M. Mirica^{*,†}

[†]Department of Chemistry, Washington University, One Brookings Drive, St. Louis, Missouri 63130-4899, United States

[‡]Department of Chemistry and Biochemistry, University of Missouri–St. Louis, One University Boulevard, Missouri 63121-4400, United States

S Supporting Information

ABSTRACT: The synthesis and structural comparison are reported herein for a series of late first-row transition metal complexes using a macrocyclic pyridinophane ligand, *N,N'*-di-*tert*-butyl-2,11-diaza[3.3](2,6)pyridinophane (^tBu₄N4). The ^tBu₄N4 ligand enforces a distorted octahedral geometry in complexes [(^tBu₄N4)M^{II}(MeCN)₂](OTf)₂ (M = Fe^{II}, Co^{II}, Ni^{II}, Cu^{II}), [(^tBu₄N4)Zn^{II}(MeCN)(OTf)](OTf), and [(^tBu₄N4)-Fe^{III}(OMe)₂](OTf), with elongated axial M–N_{amine} distances compared to the equatorial M–N_{py} distances. The geometry of [(^tBu₄N4)Cu^I(MeCN)](OTf) is pentacoordinate with weak axial interactions with the amine N-donors of ^tBu₄N4. Complexes [(^tBu₄N4)M(MeCN)₂](OTf)₂ (M = Fe, Co) exhibit magnetic properties that are intermediate between those expected for high spin and low spin complexes. Electrochemical studies of (^tBu₄N4)M complexes suggest that ^tBu₄N4 is suitable to stabilize Co^I, Ni^I, Co^{III}, Fe^{III} solvato-complexes, while the electrochemical oxidation of (^tBu₄N4)NiCl₂ complex leads to formation of a Ni^{III} species, supporting the ability of the ^tBu₄N4 ligand to stabilize first row transition metal complexes in various oxidation states. Importantly, the [(^tBu₄N4)M^{II}(MeCN)₂]²⁺ complexes exhibit two available *cis* coordination sites and thus can mediate reactions involving exogenous ligands. For example, the [(^tBu₄N4)Cu^{II}(MeCN)₂]²⁺ species acts as an efficient Lewis acid and promotes an uncommon hydrolytic coupling of nitriles. In addition, initial UV–vis and electron paramagnetic resonance (EPR) studies show that the [(^tBu₄N4)Fe^{II}(MeCN)₂]²⁺ complex reacts with oxidants such as H₂O₂ and peracetic acid to form high-valent Fe transient species. Overall, these results suggest that the (^tBu₄N4)M^{II} systems should be able to promote redox transformations involving exogenous substrates.



INTRODUCTION

Mononuclear complexes of first row transition metal ions have been extensively investigated, as they are models of a wide range of metalloenzymes.^{1,2} To achieve well-defined coordination environments that mimic metalloenzyme active sites, bioinorganic chemists have employed multidentate ligands that limit the available open coordination sites of the metal centers.³ For example, the synthesis of mononuclear metal complexes with two available *cis* coordination sites can be explored to achieve reactivity profiles with increased selectivity.⁴ In addition, use of ligands that can accommodate various geometries may promote facile redox changes that involve metal oxidation states with different geometric requirements and thus facilitate oxidative or reductive transformations.

We have recently employed flexible tetradentate N-donor ligands, *N,N'*-di-*tert*-butyl-2,11-diaza[3.3](2,6)pyridinophane (^tBu₄N4)^{5,6} and *N,N'*-dimethyl-2,11-diaza[3.3](2,6)-pyridinophane (^{Me}N4) to stabilize uncommon oxidation states of late transition metal ions and promote unprecedented reactivity.^{7–11} In particular, we have reported that ^tBu₄N4 and ^{Me}N4 effectively stabilize Pd(III) complexes and isolated the

first mononuclear organometallic Pd(III) complexes which showed unusual C–C bond formation reactivity induced by light⁷ or promoted by O₂ under mild conditions.^{8,9} The stabilization of a Pd(III) center in these complexes is likely due to the steric properties of the ^tBu₄N4 ligand and its ability to accommodate a distorted octahedral geometry preferred by a d⁷ metal center.^{7,10} In addition, the coordination compounds ^{Me}N4 with iron and vanadium have been studied previously as reactive models for catechol deoxygenases and vanadium haloperoxidases, respectively,^{12,13} while spin-transition Co and Fe complexes of both ^{Me}N4 and ^tBu₄N4 have also been reported.^{14,15} Herein, we report a series of first row transition metal complexes stabilized by ^tBu₄N4 and investigate their structural and electronic properties. Moreover, this study allows us to probe the coordination flexibility of the ^tBu₄N4 ligand to accommodate metal ions of different sizes and charges, and begin to investigate the redox reactivity of these metal complexes with two available *cis* coordination sites.

Received: December 6, 2012

Published: March 21, 2013



EXPERIMENTAL DETAILS

General Specifications. All manipulations were carried out under a nitrogen atmosphere using standard Schlenk and glovebox techniques if not indicated otherwise. All reagents for which the synthesis is not given were commercially available from Sigma-Aldrich, Acros, Strem, or Pressure Chemical, and were used as received without further purification. Solvents were purified prior to use by passing through a column of activated alumina using an MBRAUN SPS. *N,N'*-di-*tert*-butyl-2,11-diaza[3.3](2,6)pyridinophane (^tBu₄N₄),⁵ (^tBu₄N₄)-CoCl₂,⁶ and [(MeCN)₄Cu](OTf)¹⁶ were prepared according to the literature procedures. Anhydrous samples of metal triflates from Strem were used for the synthesis of the corresponding metal complexes. ¹H (300.121 MHz) NMR spectra were recorded on a Varian Mercury-300 spectrometer. Solution magnetic susceptibility measurements were obtained by the Evans method¹⁷ using coaxial NMR tubes at 293 K and 1,3,5-trimethoxybenzene or dioxane as a standard. Diamagnetic corrections were applied as previously described.¹⁸ UV–vis spectra were recorded on a Varian Cary 50 Bio spectrophotometer and are reported as λ_{max}, nm (ε, M⁻¹ cm⁻¹). Electron paramagnetic resonance (EPR) spectra were recorded on a JEOL JES-FA X-band (9.2 GHz) EPR spectrometer at 77 or 298 K. EPR spectra simulation and analysis were performed using the Bruker WINEPR SimFonia program, version 1.25. Electrospray ionization-mass spectrometry (ESI-MS) experiments were performed using a Thermo FT or Bruker Maxis Q-TOF mass spectrometer with an electrospray ionization source. Elemental analyses were carried out by the Columbia Analytical Services Tucson Laboratory. Cyclic voltammetry experiments were performed with a BASi EC Epsilon electrochemical workstation or a CHI 660D Electrochemical Analyzer. Electrochemical-grade Bu₄NBF₄ or Bu₄NClO₄ (Fluka) was used as the supporting electrolyte. Electrochemical measurements were performed in the N₂-filled glovebox or under a blanket of nitrogen, and the analyzed solutions were deaerated by purging with nitrogen. A glassy carbon disk electrode (*d* = 1.6 mm) was used as the working electrode and Ag wire pseudoreference or a Ag/0.01 M AgNO₃/MeCN electrode was used as the reference electrode. The nonaqueous reference electrode was calibrated against Cp₂Fe (Fc). Variable-temperature magnetic measurements were performed using a Quantum Design Physical Properties Measurement System in a 2–300 K temperature range under a magnetic field of 10 000 Oe (Center of Materials Innovation, Washington University). The low temperature UV–vis measurements were performed using a fiber-optic immersion probe (Hellma, path length 1 mm or 10 mm). **Caution!** Perchlorate salts are potentially explosive and should be handled with appropriate care only in small quantities.

X-ray Structure Determination. Crystals of appropriate dimensions were mounted on MiTeGen cryoloops in random orientations. Preliminary examination and data collection were performed using a Bruker Kappa Apex II or SMART Apex II Charge Coupled Device (CCD) Detector system single crystal X-ray diffractometers equipped with an Oxford Cryostream LT device. All data were collected using graphite monochromated Mo K α radiation (λ = 0.71073 Å) from a fine focus sealed tube X-ray source. Preliminary unit cell constants were determined with a set of 36 narrow frame scans. Typical data sets consist of combinations of ω and ϕ scan frames with typical scan width of 0.5° and counting time of 15–30 s/frame at a crystal to detector distance of 3.5–5.0 cm. The collected frames were integrated using an orientation matrix determined from the narrow frame scans. Apex II and SAINT software packages¹⁹ were used for data collection and data integration. Analysis of the integrated data did not show any decay. Final cell constants were determined by global refinement of *xyz* centroids from the complete data set. Collected data were corrected for systematic errors using SADABS¹⁹ based on the Laue symmetry using equivalent reflections. Crystal data and intensity data collection parameters as well as additional details of structure refinement are given in the Supporting Information. Structure solution and refinement were carried out using the SHELXTL-PLUS software package.²⁰ The structure was solved by direct methods or Patterson method and refined successfully in the space groups listed below. Full

matrix least-squares refinement was carried out by minimizing $\sum w(F_o^2 - F_c^2)^2$. The non-hydrogen atoms were refined anisotropically to convergence.

Preparation of [(^tBu₄N₄)Fe(MeCN)₂](OTf)₂. A solution of ^tBu₄N₄ (102.1 mg, 0.290 mmol) and Fe(OTf)₂ (90.0 mg, 0.254 mmol) in 17 mL of MeCN was stirred at room temperature (RT) overnight. The resulting green solution was filtered through syringe filter, evaporated to dryness, redissolved in 4 mL of MeCN and crystallized by ether vapor diffusion at –30 °C for several days. The resulting green crystals were filtered off, washed with ether and pentane, dried in an opened vial under N₂ atmosphere for 1 day without applying vacuum. Yield 157.0 mg, 78%. X-ray quality crystals were obtained by ether vapor diffusion to a concentrated MeCN solution. Anal. Found: C, 42.65; H, 4.73; N, 10.03. Calcd for C₂₈H₃₈F₆FeN₆O₆S₂: C, 42.64; H, 4.86; N, 10.66. The EA results are slightly off likely because of MeCN solvent loss during the shipping and handling of the solid sample.

Preparation of [(^tBu₄N₄)Co(MeCN)₂](OTf)₂. A solution of AgOTf (91.0 mg, 0.354 mmol, 2 equiv) in 3 mL of MeCN was added to a stirred blue suspension of (^tBu₄N₄)CoCl₂ (85.5 mg, 0.177 mmol) in 4.5 mL of MeCN. When addition of AgOTf was complete, white clumps of AgCl precipitate from solution. The reaction mixture was stirred at RT for 20–30 min, then left to stand without stirring for 30 min. The reaction mixture was filtered through Celite, the resulting red solution was evaporated to dryness, and the solid red residue was recrystallized by ether vapor diffusion to concentrated MeCN solution overnight. The crystalline product was filtered off, washed with ether, pentane. Yield 55.4 mg, 39%. An additional fraction of the product can be obtained by concentrating the filtrate and recrystallization from MeCN-ether at –30 °C. X-ray quality crystals were obtained by ether vapor diffusion to a concentrated CH₂Cl₂ solution at RT. ESI-MS of MeCN solution of [(^tBu₄N₄)Co(MeCN)₂](OTf)₂, *m/z* 205.6000 (calcd for [(^tBu₄N₄)Co]²⁺, [C₂₂H₃₂N₄Co]²⁺, *m/z* 205.5979), *m/z* 226.1127 (calcd for [(^tBu₄N₄)Co(MeCN)]²⁺, [C₂₄H₃₅N₅Co]²⁺, *m/z* 226.1112). Anal. Found: C, 42.72; H, 4.79; N, 10.40. Calcd for C₂₈H₃₈CoF₆N₆O₆S₂: C, 42.48; H, 4.84; N, 10.62.

Preparation of (^tBu₄N₄)NiCl₂. A suspension of NiCl₂·6H₂O (40.4 mg, 0.170 mmol) and ^tBu₄N₄ (62.1 mg, 0.176 mmol) in CH₂Cl₂-MeCN mixture (10 mL/10 mL) was stirred at room temperature. All solids dissolved after 1 h. After stirring for 24 h, solvents were removed by rotary evaporation, and the resulting green solid was redissolved in a minimum of MeCN and crystallized by ether vapor diffusion into MeCN solution. Large green crystals were filtered off, washed with ether and pentane, and dried under vacuum. Yield 61.1 mg, 79%. Green crystalline solid, soluble in MeCN, dichloromethane. X-ray quality crystals of (^tBu₄N₄)NiCl₂ were obtained by ether diffusion to concentrated MeCN solution at RT. ¹H NMR (CD₃CN, 25 °C, 300 MHz), δ : 62.3, 24.0, 16.3, –5.31 (br). ESI-MS of MeCN-MeOH solution of (^tBu₄N₄)NiCl₂, *m/z* 445.1663 (calcd for (^tBu₄N₄)NiCl₂⁺, C₂₂H₃₂N₄NiCl₂⁺, *m/z* 445.1663), *m/z* 205.0986 (calcd for (^tBu₄N₄)Ni²⁺, C₂₂H₃₂N₄Ni²⁺, *m/z* 205.0985). Anal. Found: C, 54.02; H, 6.97; N, 11.34. Calcd C₂₂H₃₂Cl₂N₄Ni: C, 54.81; H, 6.69; N, 11.62.

Preparation of [(^tBu₄N₄)Ni(MeCN)₂](OTf)₂. A solution of AgOTf (100.6 mg, 0.392 mmol, 2 equiv) in 5 mL of MeCN was added to a stirred solution of (^tBu₄N₄)NiCl₂ (95.3 mg, 0.198 mmol) in 10 mL of MeCN. Stirring continued at RT in the dark. After 30 min, solution was filtered through a 0.2 μ m syringe filter to remove white precipitate of AgCl. The resulting pink-purple solution was evaporated to dryness, redissolved in 1–2 mL of MeCN and recrystallized by ether vapor diffusion overnight. Large purple crystals were filtered off, washed with ether, pentane, and stored at –20 °C. Yield 123.4 mg, 79%. X-ray quality crystals were obtained by ether vapor diffusion into MeCN solution of [(^tBu₄N₄)Ni(MeCN)₂](OTf)₂. ESI-MS of MeCN solution of [(^tBu₄N₄)Ni(MeCN)₂](OTf)₂, *m/z* 600.1760 (calcd for [(^tBu₄N₄)-Ni(MeCN)₂]²⁺, C₂₅H₃₅N₅NiF₃SO₃⁺, *m/z* 600.1761), *m/z* 559.1494 (calcd for [(^tBu₄N₄)Ni]²⁺, C₂₂H₃₂N₄NiF₃SO₃⁺, *m/z* 559.1495), *m/z* 225.6118 (calcd for [(^tBu₄N₄)Ni(MeCN)]²⁺, C₂₄H₃₅N₅Ni²⁺, *m/z* 225.6117). Anal. Found: C, 40.71; H, 4.97; N, 8.62. Calcd for ^tBu₄N₄Ni(OTf)₂·2MeCN (C₂₈H₃₈F₆N₆NiO₆S₂): C, 42.49; H, 4.84; N, 10.62; ^tBu₄N₄Ni(OTf)₂ (C₂₄H₃₂F₆N₄NiO₆S₂): C, 40.64; H, 4.55; N,

7.90. The EA results are slightly off likely because of MeCN solvent loss during the shipping and handling of the solid sample.

Preparation of [(^tBuN4)Cu(MeCN)₂](OTf)₂. A solution of ^tBuN4 (47.8 mg, 0.135 mmol) and Cu(OTf)₂ (49.0 mg, 0.135 mmol) in 10 mL of MeCN was stirred at RT overnight. The blue solution was evaporated to dryness, and the solid residue was redissolved in 1–2 mL of MeCN and crystallized by ether layering at –30 °C. The resulting blue crystals were filtered off, washed with ether, pentane. Yield 82.5 mg, 77%. X-ray quality crystals were obtained by ether vapor diffusion to a concentrated MeCN solution at RT. ESI-MS of MeCN solution of [(^tBuN4)Cu(MeCN)₂](OTf)₂, *m/z* 207.5972 (calcd for [(^tBuN4)Cu]²⁺, C₂₂H₃₂N₄Cu²⁺, *m/z* 207.5961), *m/z* 564.1427 (calcd for [(^tBuN4)Cu](OTf)⁺, C₂₃H₃₂N₄CuF₃SO₃⁺, *m/z* 564.1443). Evans method, CD₃CN solution, 293 K: $\mu_{\text{eff}} = 2.11 \mu_{\text{B}}$. Anal. Found: C, 41.55; H, 5.32; N, 10.08. Calcd for ^tBuN4Cu(OTf)₂·2MeCN (C₂₈H₃₈CuF₆N₆O₆S₂): C, 42.23; H, 4.81; N, 10.55; ^tBuN4Cu(OTf)₂·MeCN (C₂₆H₃₅CuF₆N₆O₆S₂): C, 41.35; H, 4.67; N, 9.27. The EA results are slightly off likely because of MeCN solvent loss during the shipping and handling of the solid sample.

Preparation of [(^tBuN4)Zn(MeCN)(OTf)](OTf). A solution of ^tBuN4 (47.5 mg, 0.135 mmol) and Zn(OTf)₂ (49.0 mg, 0.135 mmol) in 10 mL of MeCN was stirred at RT overnight. Colorless solution was evaporated to dryness, and the white solid residue was redissolved in 1–2 mL of MeCN and crystallized by ether layering at –30 °C. The resulting white powder was filtered off, washed with ether, pentane. Yield 80.3 mg, 78%. X-ray quality crystals were obtained by ether vapor diffusion to a concentrated MeCN solution at –30 °C. ¹H NMR (CD₃CN, 25 °C, 300 MHz), δ : 1.42 (s, 18H, tBu), 3.50 (d, *J* = 17.1 Hz, 4H, CH₂), 4.63 (d, *J* = 17.1 Hz, 4H, CH₂), 7.33 (d, *J* = 7.8 Hz, 4H, Py C_{meta}-H), 7.89 (t, *J* = 7.8 Hz, 2H, Py C_{para}-H). Anal. Found: C, 40.27; H, 5.50; N, 7.83. Calcd for [(^tBuN4)Zn(OTf)]₂·2MeCN (C₂₈H₃₈F₆N₆O₆S₂Zn): C, 42.13; H, 4.80; N, 10.53. Calcd for (^tBuN4)Zn(OTf)₂ (C₂₄H₃₂F₆N₄O₆S₂Zn): C, 40.26; H, 4.50; N, 7.82. The EA results are slightly off likely because of MeCN solvent loss during the shipping and handling of the solid sample.

Preparation of [(^tBuN4)Cu(MeCN)](OTf). Solid samples of ^tBuN4 (49.2 mg, 0.140 mmol) and [Cu(MeCN)₄](OTf) (52.6 mg, 0.140 mmol) were dissolved in 2 mL of CH₂Cl₂, and the resulting yellow solution was stirred at RT for 10–15 min, filtered through a cotton plug, and crystallized by ether vapor diffusion at RT and then at –30 °C. The yellow crystalline product was filtered off, washed with ether, pentane. Yield 60.8 mg, 72%. Anal. Found: C, 50.50; H, 6.05; N, 12.37. [(^tBuN4)Cu(MeCN)](OTf)·MeCN (C₂₇H₃₈CuF₃N₆O₃S): C, 50.10; H, 5.92; N, 12.98.

Preparation of (^tBuN4)Fe(OTf)₂. A green crystalline sample of [(^tBuN4)Fe(MeCN)₂](OTf)₂ (66.6 mg, 0.084 mmol) was finely ground in an agate mortar, and the powder sample was dried under high vacuum at RT for 10 h until the mass of the sample was constant. The product was obtained as a pale yellow powder, yield 59.7 mg (0.084 mmol), quantitative yield. X-ray quality crystals were obtained by ether vapor diffusion to a concentrated solution in THF-CH₂Cl₂ (1:1 v:v). Anal. Found: C, 41.02; H, 4.45; N, 7.77. Calcd for C₂₄H₃₂F₆FeN₄O₆S₂: C, 40.80; H, 4.57; N, 7.93.

Preparation of [(^tBuN4)Fe(OMe)₂](OTf). To a solution of [(^tBuN4)Fe(MeCN)₂](OTf)₂ (60.1 mg, 0.076 mmol) in 5 mL of degassed MeOH cooled down to –35 °C was added first Et₃N (53 μ L, 5 equiv), then 50% wt. aq. H₂O₂ (44 μ L, 10 equiv) to give a bright yellow solution. The reaction mixture was stirred at –35 °C for 10–15 min, then at RT for 3 h. The solution was evaporated to dryness, the yellow crystalline solid was redissolved in 0.5 mL of MeCN and precipitated with 5 mL of ether at –20 °C. Yellow crystals were filtered off, washed with ether, pentane, and dried under vacuum to give 29.3 mg of the product as yellow crystalline solid. An additional fraction of the product was obtained by precipitation from the filtrate with an additional 5 mL of ether, yield 8.3 mg. Combined yield 37.6 mg, 80%, yellow crystalline solid. X-ray quality crystals were obtained by ether diffusion to concentrated MeCN solution at –20 °C. UV–vis, λ , nm (ϵ , L·mol^{–1}·cm^{–1}), MeOH: br 310 (13 000), 257 (23 800). ESI-MS of MeOH solution of [(^tBuN4)Fe(OMe)₂](OTf), *m/z* 470.2372 (calcd for [(^tBuN4)Fe(OMe)₂]⁺, C₂₄H₃₈N₄O₂Fe, *m/z* 470.2339). Evans method,

CD₃OD solution, 293 K: $\mu_{\text{eff}} = 1.61 \mu_{\text{B}}$. Anal. Found: C, 47.78; H, 6.77; N, 8.92. Calcd for [(^tBuN4)Fe(OMe)₂](OTf)·MeOH (C₂₆H₄₂F₃FeN₄O₆S): C, 47.93; H, 6.50; N, 8.60.

Electrolysis of (^tBuN4)NiCl₂. A solution of 7.7 mg of (^tBuN4)NiCl₂ in 8 mL of 0.1 M Bu₄NClO₄ in CH₂Cl₂ was placed into a working chamber of the H-shape electrolysis cell. The auxiliary chamber was filled with 8 mL of 0.1 M Bu₄NClO₄/CH₂Cl₂. The electrolysis was performed in a stirred solution at 805 mV vs Fc⁺/Fc using a platinum mesh working electrode, AgNO₃/Ag/MeCN reference electrode and platinum mesh auxiliary electrode. After the charge corresponding to one-electron oxidation of the complex has passed, the current dropped more than 20-fold compared to the current at the beginning of electrolysis, and the electrolysis was stopped. CV recorded after electrolysis shows a quasireversible reduction wave at the same potentials as the oxidation wave for the starting material. The UV–vis spectrum of the resulting brown solution was recorded immediately. The solution was stored at –20 °C overnight to give dark-brown solid product that was analyzed by EPR. The UV–vis spectrum of the isolated solid product redissolved in CH₂Cl₂ is identical to the UV–vis spectrum of the solution recorded immediately after electrolysis. The complex is moderately stable in the solid state at low temperatures and decomposes in solution at room temperature over the course of several hours. UV–vis, λ , nm (ϵ , L·mol^{–1}·cm^{–1}), CH₂Cl₂: 266 (12 500), sh 296 (7110), sh 342 (3250), 397 (3410), sh 497 (1310), sh 608 (415), 968 (292).

Preparation of 9, [(^tBuN4)Cu(OCMeNHCMENH)](ClO₄)₂. A solution of ^tBuN4 (50.5 mg, 0.143 mmol) and Cu(ClO₄)₂·6H₂O (53.1 mg, 0.143 mmol) in 17 mL of MeCN was stirred under air for 2 days. The blue-green solution was filtered through Celite, evaporated to dryness, and recrystallized twice by ether vapor diffusion to a solution in MeCN (2–3 mL). Large blue-green plates were filtered off, washed with ether, pentane, dried under vacuum. Yield 65.5 mg, 56%. X-ray quality crystals were obtained by ether vapor diffusion to a concentrated MeCN solution at RT. UV–vis, λ , nm (ϵ , L·mol^{–1}·cm^{–1}), CH₃CN: 263 (23 100), sh 367 (240), 640 (29). Evans method, CD₃CN solution, 293 K: $\mu_{\text{eff}} = 1.93 \mu_{\text{B}}$. FT-IR (KBr pellet): 3380, 3250 cm^{–1} (br, NH stretches).

RESULTS AND DISCUSSION

Synthesis. The synthesized (^tBuN4)M complexes (M = Fe, Co, Ni, Cu, Zn) are listed in Chart 1. The bis-acetonitrile complexes [(^tBuN4)M(MeCN)₂](OTf)₂ where M = Fe (1) or Cu (4) were synthesized in 70–80% yield by reacting 1 equiv of ^tBuN4 with the corresponding anhydrous metal triflate salt, Fe(OTf)₂ or Cu(OTf)₂, in MeCN (eq 1). The reaction of Ni(OTf)₂ with ^tBuN4 failed to produce the desired complex because of the poor solubility of the triflate precursor. The complex [(^tBuN4)Ni(MeCN)₂](OTf)₂ (3) was conveniently synthesized by chloride abstraction by 2 equiv of AgOTf from (^tBuN4)NiCl₂ (7, eq 2), which was obtained through reaction of nickel chloride with 1 equiv of ^tBuN4 in CH₂Cl₂/MeCN. A similar procedure was used for the preparation of [(^tBuN4)Co(MeCN)₂](OTf)₂ (2) from (^tBuN4)CoCl₂ (eq 2).⁶ The product obtained by the reaction of Zn(OTf)₂ with ^tBuN4 in MeCN was found to be a monoacetonitrile monotriflate complex [(^tBuN4)Zn(MeCN)(OTf)](OTf) (5) in the solid state, according to the X-ray analysis (eq 3). The NMR spectrum of 5 reveals a symmetrical species in solution that exhibits only two doublets of the CH₂ groups and one triplet of para-H of pyridine rings, likely because of the formation of a more symmetrical [(^tBuN4)Zn(MeCN)₂]²⁺ species in solution or a fast exchange between OTf and MeCN ligands. The Cu^I complex [(^tBuN4)Cu^I(MeCN)](OTf) (6) was obtained by the reaction of [Cu^I(MeCN)₄](OTf) precursor with 1 equiv of ^tBuN4 in CH₂Cl₂ under N₂ (eq 4). All complexes were isolated and purified by recrystallization and characterized by

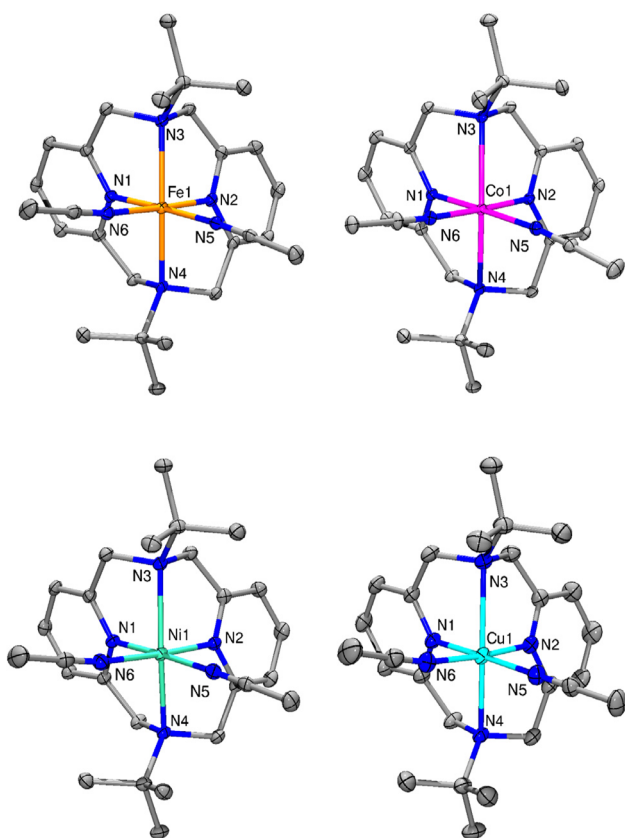


Figure 1. ORTEP plots (50% probability ellipsoids) for the cations of 1–4.

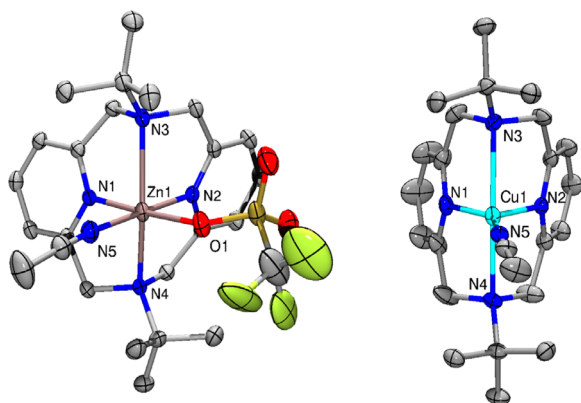


Figure 2. ORTEP plots (50% probability ellipsoids) for the cations of 5 and 6.

elongated $M-N_{\text{amine}}$ bond lengths compared to complexes 1–3 and 5, and this can be attributed to a tetragonally distorted octahedral geometry characteristic for d^9 ions.

Interestingly, the $M-N$ distances in the dicationic complexes 1–4 are considerably shorter compared to neutral dichloro-analogues, which is especially significant for Fe(II) and Co(II) complexes.⁶ For comparison, the average $M-N_{\text{py}}$ and $M-N_{\text{amine}}$ bond distances for acetonitrile complexes 1–5 and dichloro complexes are shown in Tables 2 and 3, respectively. Moreover, while the average $M-N_{\text{py}}$ and $M-N_{\text{amine}}$ bond distances for dichloro complexes decrease along the series from Fe to Co to Ni correlating with decrease of the ionic radii for high spin complexes,⁶ a different trend is observed for complexes 1–3. Although the average $M-N$ bond distances

Table 2. Average $M-N$ Bond Distances in Complexes 1–5

	1 ^a	2 ^a	3 ^a	4 ^b	5 ^b
$M-N_{\text{py,ave}}$	1.8989	1.9114	1.9807	1.9890	2.039
$M-N_{\text{am,ave}}$	2.1489	2.3154	2.2586	2.4075	2.336
$M-N_{\text{MeCN,ave}}$	1.9457	1.9215	2.0509	2.0085	-
$M-N_{\text{ave}}$	1.9978	2.0495	2.0967	2.1350	2.169

^a100 K. ^b173 K.

Table 3. Average $M-N$ Bond Distances in Complexes 1 at 293 and 173 K and 2 at 296 K

	1 (293 K)	1 (173 K)	2 (296 K)
$M-N_{\text{py(ave)}}$	1.908	1.9006	1.928
$M-N_{\text{am(ave)}}$	2.165	2.1520	2.330
$M-N_{\text{MeCN(ave)}}$	1.952	1.9473	1.941
$M-N_{\text{ave}}$	2.008	2.0000	2.067

for all types of N-donor atoms including MeCN increase along the series for complexes 1–3, no clear trend is seen when the average $M-N_{\text{py}}$, $M-N_{\text{amine}}$, and $M-N_{\text{MeCN}}$ distances are compared. Interestingly, although the $M-N$ bond distances in Fe(II) and Co(II) complexes 1 and 2 are in a range expected for low-spin complexes, the SQUID measurements and determination of the effective magnetic moments in solution by the Evans method give values that are intermediate between those expected for low spin and high spin complexes (vide infra). The X-ray structures determined at variable temperatures (100, 173, and 293 K for 1 and 100 and 296 K for 2) reveal similar unit cell parameters and only a slight elongation of $M-N$ bond distances at room temperature for both 1 and 2 compared to the structures at 100 K (Table 4), which could be

Table 4. Average $M-N$ Bond Distances (Å) for Dichloride Complexes (^tBu₄N₄)MCl₂

	(^t Bu ₄ N ₄)FeCl ₂	(^t Bu ₄ N ₄)CoCl ₂	(^t Bu ₄ N ₄)NiCl ₂ ^a
$M-N_{\text{py,ave}}$ (Å)	2.146	2.089	2.016
$M-N_{\text{am,ave}}$ (Å)	2.436	2.406	2.324
$M-N_{\text{ave}}$ (Å)	2.291	2.247	2.170

^aAverage for the two independent molecules found in the unit cell of 7.

due to selective crystallization of only low-spin species under these conditions. Notably, Fe–N distances in complex 8 (Supporting Information, Figure S33) are within a normal range for high-spin Fe(II) complexes²² consistent with the magnetic properties of this complex (vide infra). In addition, $\text{Co}-N_{\text{py(ave)}}$ distances for complex 2 are similar to those reported by Krüger et al. for a (^tBu₄N₄)Co(II) semiquinonate complex that shows a spin transition from low spin to high spin above 200 K that is not complete even at 400 K.¹⁵

The X-ray structure of Cu(I) complex 6 reveals strong coordination of two pyridine rings of ^tBu₄N₄ ligand and only one MeCN ligand and much weaker interactions with two axial amines ($\text{Cu}-N_{\text{amine}}$ 2.416 and 2.487 Å). The structural parameter τ calculated for a five-coordinate complex 6 is 0.03,²³ indicating that the ligand arrangement may be formally considered as a distorted square pyramidal rather than trigonal bipyramidal, with a basal plane formed by MeCN, one pyridine, and two amines and another pyridine in an apical position, although the Cu–amine distances are much longer compared with both $\text{Cu}-N_{\text{py}}$ and $\text{Cu}-N_{\text{MeCN}}$ bond distances. Notably,

Table 5. Selected Physical Properties of Complexes 1–8

1	2	3	4	5	6	7	8
4.42 ^a	3.06 ^a	3.46 ^a	2.11 ^a	NA	NA	3.20 ^a	5.25 ^b
$\mu_{\text{eff}} (\mu_{\text{B}})$ at 293 K, Evans method							
UV-vis, λ_{max} nm (ϵ , M ⁻¹ cm ⁻¹)							
br 246 (15500), 354 (2080), 396 (2260), 669 (32) ^c	244 (21100), 308 (1670), sh 340 (1160), 420 (53), sh 500 (30), 930 (33) ^c	259 (11600), sh 340 (176), 514 (7), 625 (5), 755 (7), 1030 (36) ^c	261 (22 800), sh 373 (133), 634 (29) ^c	264 (16200), sh 274 (10600), sh 315 (177) ^c	249 (14300), 263 (12 200), sh 300 (6000), 365 (1690) ^d	261 (12500), 354 (160), 615 (7), 913 (7) ^d	265 (14800), 340 (4220) ^e

^aIn CD₃CN. ^bIn acetone-d₆. ^cIn MeCN. ^dIn CH₂Cl₂. ^eIn THF. NA: not applicable.

Table 6. Electrochemical Properties of Complexes 1–7 (V vs. Fc⁺/Fc)^a

1	2	3	4	5	6	7
$E_{\text{pc1}} -1.77$ (irrev); $E_{\text{pc2}} -2.05$ (irrev) $E_{\text{pa}} +0.73$ (quasirev) ^b	$E_{1/2} -1.50$ (quasirev, $\Delta E_{\text{p}} 68$ mV); $E_{\text{pc2}} -2.05$ (quasirev); $E_{1/2} +0.30$ (quasirev, $\Delta E_{\text{p}} 80$ mV) ^c	$E_{1/2} -1.35$ (quasirev, $\Delta E_{\text{p}} 90$ mV); $E_{\text{pc2}} -1.82$ (irrev) $E_{\text{pa}} +1.64$ (irrev) ^b	$E_{\text{pc}} -0.55$; $E_{\text{pa}} 0.00$ ^{b,d}	$E_{\text{pc1}} -2.14$ (irrev); $E_{\text{pc2}} -2.26$ (irrev) ^b	$E_{\text{pa}} -0.50$; $E_{\text{pc}} +0.01$ ^{b,e}	$E_{1/2} +0.52$ (quasirev, $\Delta E_{\text{p}} 125$ mV) ^f

^aIn 0.1 M Bu₄NBF₄/MeCN; potentials are reported in V vs Fc⁺/Fc; ΔE_{p} is the separation between anodic and cathodic waves in mV. ^bMeasured at 100 mV/s. ^cMeasured at 500 mV/s. ^dThe anodic wave E_{pa} appears only after the initial cathodic scan. ^eThe cathodic wave E_{pc} appears only after the initial anodic scan. ^fIn 0.1 M Bu₄NClO₄/MeCN.

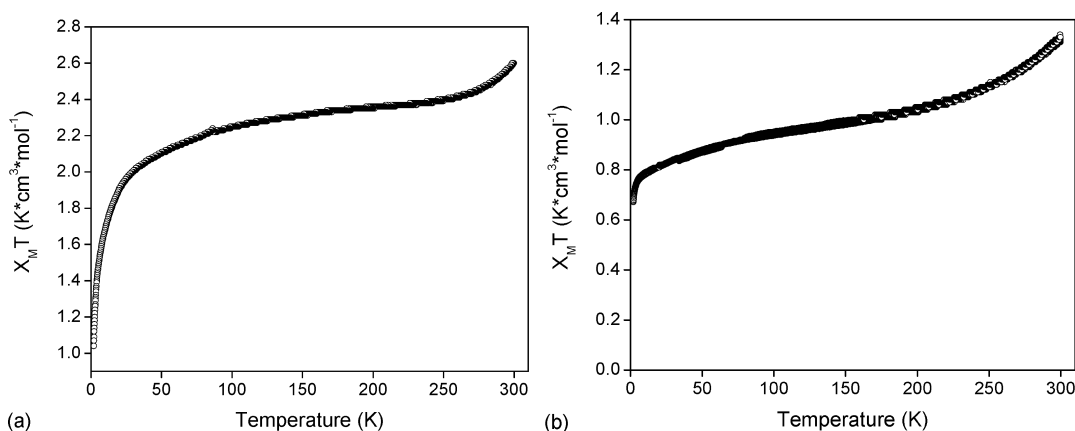


Figure 3. Solid-state SQUID data for complex 1 (a) and for complex 2 (b).

the ^tBuN4 coordination in complex 6 is less “twisted” compared with that in complexes 1–4, and the pyridine rings are almost perpendicular to the equatorial plane of the complex (the angles between the average plane of pyridine rings and a mean equatorial plane are 85.02° and 86.34°). For comparison, the angles between the average plane of pyridine rings and the equatorial plane for complex 4 are 75.61° and 75.73°. Such more symmetrical macrocycle ring coordination is likely due to the significantly elongated Cu–N_{amine} bond distances. Overall, the ^tBuN4 ligand coordination mode is similar for Cu complexes in two different oxidation states, 6 and 4, with two short Cu–N_{py} and two elongated Cu–N_{amine} distances, while only the number of MeCN ligands is different between the two oxidation states.

In the solid state, the zinc complex 5 was found to have one MeCN and one triflate ligand bound in the equatorial plane of the metal center (Figure 2). Several crystals picked up from the reaction mixture showed identical structures, and the expected species containing two MeCN molecules coordinated to the metal center, analogous to 1–4, could not be found in the crystalline sample. The geometry of a metal center of 5 is highly distorted octahedral with considerably different Zn–N_{amine} distances of 2.366 and 2.307 Å.

Magnetic Properties. The selected physical properties of complexes 1–8 are summarized in Table 5. The effective magnetic moments measured in MeCN or acetone by the

Evans method at RT for the Fe(II) complex 8 and the Ni(II) complexes 3 and 7 are consistent with the values expected for high-spin octahedral complexes.²⁴ The magnetic moment of 2.11 μ_{B} for 4 is consistent with a d⁹ Cu(II) center,²⁴ and its EPR spectrum reveals an axial signal with $g_{\perp} = 2.055$ and $g_{\parallel} = 2.258$ ($A_{\parallel} = 173$ G) consistent with a tetragonally elongated octahedral Cu(II) d⁹ center (Supporting Information, Figure S20).

By comparison, a more complicated magnetic behavior was observed for Fe(II) and Co(II) complexes 1 and 2. The μ_{eff} value of 4.42 μ_{B} determined by the Evans method for 1 in MeCN is lower than the spin-only magnetic moment for high spin Fe(II) complex (4.90 μ_{B}), suggesting that both high spin and low spin are likely present in solution at RT. The SQUID measurements for a finely ground solid sample of 1 give a $\chi_{\text{M}} \cdot T$ value of 2.55 T·cm³·mol⁻¹ at 293 K, corresponding to a μ_{eff} of 4.52 μ_{B} , lower than the value expected for high spin Fe(II) complexes²⁵ and consistent with the Evans method results obtained in solution at 293 K. Variable temperature SQUID measurements reveal that $\chi_{\text{M}} \cdot T$ decreases gradually and does not have a well-defined plateau region (Figure 3, a), suggesting that the spin transition is incomplete between 300 and 2 K or intermediate spin states are present.²² The observed features were reproducible for two independently prepared samples of 1. The effective magnetic moment measured by the Evans method for Co(II) complex 2 in MeCN, 3.06 μ_{B} , is also lower

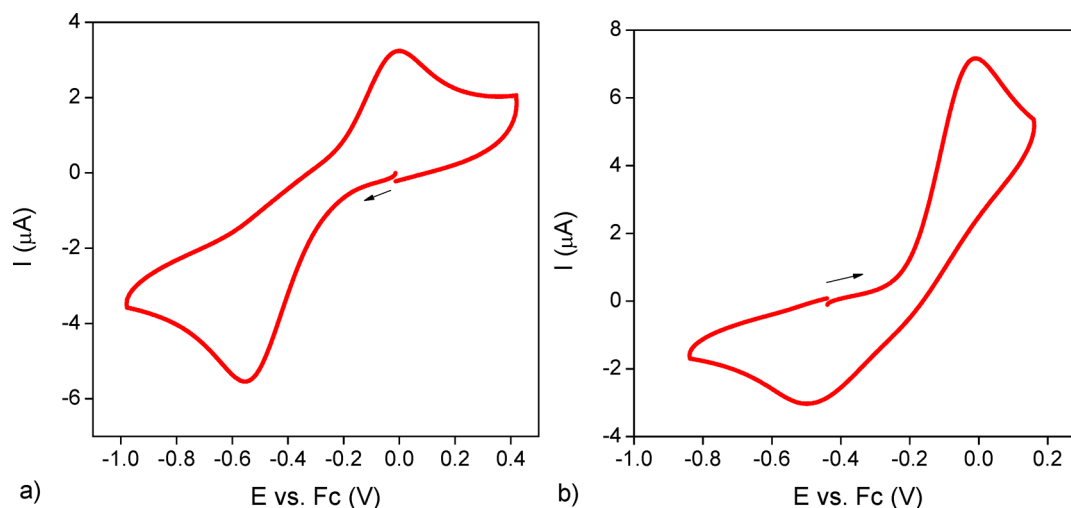


Figure 4. (a) CV of the Cu(II) complex **4**. (b) CV of the Cu(I) complex **6** (0.1 M Bu₄NBF₄/MeCN, $\nu = 100$ mV/s; arrow indicates the initial scan direction).

than the spin-only μ_{eff} expected for high spin Co(II) ($3.88 \mu_{\text{B}}$). The SQUID measurements for the solid sample of **2** give $\chi_{\text{M}}T$ value of $1.29 \text{ K}\cdot\text{cm}^3\cdot\text{mol}^{-1}$ corresponding to μ_{eff} of $3.21 \mu_{\text{B}}$, lower than expected value for high spin Co(II) complex and higher than the value expected for low spin Co(II) species (Figure 3, a). The variable temperature SQUID data reveal gradually decreasing $\chi_{\text{M}}T$ over the temperature range of 300 to 2 K without a well-defined plateau region, suggestive of an incomplete spin transition (Figure 3, b).²⁶ While no clearly defined spin transitions were observed for **1** and **2** by SQUID in the temperature range employed, their $\chi_{\text{M}}T$ values gradually increase at temperatures higher than RT, suggesting that at RT both **1** and **2** exhibit magnetic properties and μ_{eff} values that are intermediate between those expected for high spin and low spin complexes.^{22,26} Because of the complex magnetic behavior of complexes **1** and **2** and the inability to achieve a temperature at which the spin transition was complete, several attempts to simulate the SQUID data proved to be difficult and did not provide acceptable fits.^{14,15}

Similarly, Krüger et al. reported that a Co(II) semiquinonate complex supported by the ^tBuN4 ligand undergoes a gradual thermally induced low spin to high spin transition between 200 and 400 K, and variable temperature X-ray studies reveal elongation of Co–N_{py(ave)} bonds from 1.931 Å at 100 K to 1.991 Å at 400 K.¹⁵ Thus, structural parameters for complex **2** are similar to those for the Co(II) complex reported by Krüger et al.¹⁵ Moreover, Fe(III) complex with an analogous ^MeN4 ligand was shown by the same group to undergo a thermally induced transition from low spin to intermediate spin state ($S = 3/2$), which was attributed to a highly distorted octahedral geometry imposed by ^MeN4 ligand coordination with strong M–N_{py} and weak M–N_{amine} interactions.¹⁴ Overall, the unusual magnetic properties for complexes **1** and **2** could also be attributed to incomplete transition between low spin and high spin species imposed by the presence of ^tBuN4 and MeCN ligands,²² while no such behavior was observed for the analogous (^tBuN4)Fe(OTf)₂ (**8**), (^tBuN4)NiCl₂ (**8**), and (^MeN4)MCl₂ (M = Co, Ni)²¹ complexes with weaker field triflate or chloride ligands, all of which exhibit effective magnetic moments and structural parameters typical for the high spin octahedral complexes.

UV–vis Properties. The UV–vis spectrum of Zn complex **5** in MeCN solution reveals an intense ligand-based transition at 264 nm, similar to the absorption observed in the spectrum of the free ligand at 264 nm ($\epsilon = 10\,700 \text{ M}^{-1} \text{ cm}^{-1}$) and was assigned as an ligand-based absorption, which was also observed for all other (^tBuN4)M complexes **1–7**. In addition to ligand-based absorptions, the Cu(I) complex **6** also reveals two intense bands at 300 and 365 nm that were assigned as Cu(I)-to-pyridine metal-to-ligand charge-transfer (MLCT) transitions, while **4** exhibits a d-d transition at 634 nm as expected for a distorted octahedral Cu(II) complex.²⁷ Three low intensity bands in the visible region at 930, 500, and 420 nm were observed for the Co(II) complex **2** and correspond to the ⁴T_{1g} → ⁴T_{2g}, ⁴T_{1g} → ⁴A_{2g}, and ⁴T_{1g} → ⁴T_{2g} (P) transitions, respectively, while the more intense absorptions at ~340 and 308 nm are likely MLCT bands.²⁷ The UV–vis spectra of the Ni(II) complexes **3** and **7** exhibit weak d-d transitions in the 600–1000 nm range, typical for distorted octahedral Ni(II) centers, in addition to the ligand-based transitions at ~260 nm and MLCT bands at ~340 nm.²⁷ Finally, a MeCN solution of **1** exhibits a distinct d-d transition at 669 nm that is responsible for the characteristic green color of the solution, in addition to two intense MLCT bands at 354 and 396 nm. By contrast, the solution of the high-spin complex (^tBuN4)Fe(OTf)₂ **8** in THF exhibits a ligand-based absorption band at 265 nm and a charge transfer band at 340 nm, while no d-d transitions were present in the visible region.

Electrochemical Properties. The electrochemical properties of complexes **1–8** are summarized in Table 6. The Zn complex **5** was examined to probe the redox reactivity of the ^tBuN4 ligand when bound to a metal center. No ligand oxidation was observed at anodic potentials up to +1.7 V vs Fc⁺/Fc, while the cathodic scan revealed two ligand-based irreversible reductions at –2.14 V and –2.26 V vs Fc⁺/Fc, respectively (Table 6 and Supporting Information, Figure S1), suggesting that the ^tBuN4 ligand is redox innocent over a large potential range.

The cyclic voltammogram (CV) of the Cu(II) complex **4** features a quasireversible reduction wave at –0.55 V with a large separation between the cathodic wave and the corresponding anodic wave at 0.00 V vs Fc⁺/Fc (Figure 4, a). Accordingly, the CV of the Cu(I) complex **6** shows a quasi-

reversible oxidation wave at +0.01 V and the corresponding reduction wave at -0.50 V at the potentials similar to those determined for the Cu(II) complex 4, thus confirming that species 6 and 4 likely interconvert during the electrochemical oxidation/reduction in MeCN (Figure 4, b). The peak potential of the cathodic wave for complex 4 and the peak potential of the anodic wave for complex 6 shift by ~60 mV and ~65–80 mV, respectively, upon 10-fold increase of the scan rate (Supporting Information, Figures S5 and S6),²⁸ consistent with a slow electron transfer step.²⁹ This could be due to the structural reorganization of the ^tBuN4 ligand and coordination/decoordination of one MeCN ligand that occurs during Cu^{II}/Cu^I interconversion.³⁰ The redox potentials of complexes 4 and 6 are similar to those reported for the Cu(II) acetonitrile complex with a rigid bispidine ligand that possesses two pyridine and two amine donors and similarly shows a large separation between the forward cathodic and the reverse anodic wave, likely because of the rigidity of the ligand system.³¹ By contrast, pentacoordinate Cu(II) and Cu(I) monoacetonitrile complexes [(TMPA)Cu(MeCN)]²⁺ and [(TMPA)-Cu^I(MeCN)]⁺ with the tetradentate pyridine/amine donor ligand tris(2-pyridylmethyl)amine (TMPA) show a quasireversible one-electron wave with a much smaller peak-to-peak separation ΔE_p of 87–91 mV, likely because of a greater flexibility of the TMPA ligand and a presence of a formally pentacoordinate metal center for both Cu(II) and Cu(I) centers.³²

Complexes 1–3 exhibit two reduction waves, one at significantly less negative potentials compared to the Zn complex 5 that are likely due to metal-based reductions, while the second reduction wave for complexes 1 and 2 is comparable to that observed for 5 and could be due to either a ligand-based or a metal-based reduction.

The first reduction wave is quasireversible for complexes 2 ($\Delta E_p = 68$ mV) (Figure 5) and 3 ($\Delta E_p = 90$ mV) and was

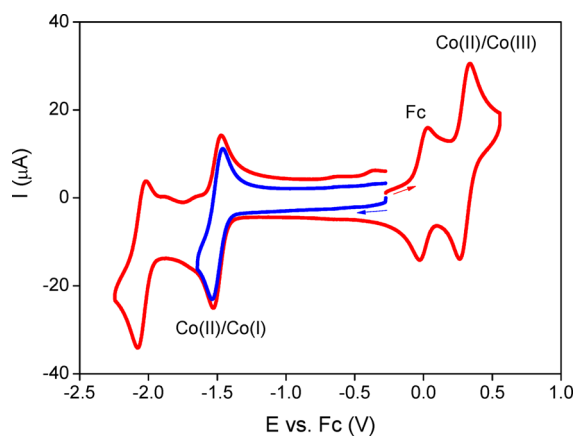


Figure 5. CV of the Co(II) complex 2 (in the presence of Fc): blue, cathodic scan for the first reduction wave; red, initial anodic scan followed by the full cathodic scan ($\text{Bu}_4\text{NBF}_4/\text{MeCN}$, $\nu = 500$ mV/s; arrow indicates the initial scan direction).

assigned as a one-electron $\text{M}^{\text{II}}/\text{M}^{\text{I}}$ reduction. The quasireversibility of this reduction wave indicates that a one-electron reduced state may be accessible for these complexes. By comparison, the reduction wave for Fe(II) complex 1 is observed at a significantly more negative potential compared to 2 and 3 and remains irreversible even at higher scan rates likely because of instability of the reduced species.

Complex 2 shows a quasireversible oxidation wave at +0.30 V vs Fc⁺/Fc assigned as a Co^{II}/Co^{III} oxidation (Figure 5). The peak currents and the anodic/cathodic wave separations for the Co^{II}/Co^{III} oxidation Co^{II}/Co^I reduction are comparable and correspond to one-electron redox processes. Compared to a structurally similar Co(II) complex with a tetradentate pyridine donor PY4 ligand, the reduction wave of complex 2 is only slightly more negative and the oxidation wave is more positive compared to [(PY4)Co(MeCN)₂]²⁺.³³

The oxidation of Fe(II) the complex 1 is irreversible at slow scan rates; however, the corresponding reverse wave becomes more intense at scan rates exceeding 500 mV/s (Supporting Information, Figure S3),²⁸ consistent with the presence of irreversible chemical transformations following the electrochemical oxidation.

The dicationic Ni(II) complex 3 also shows an irreversible oxidation wave at a high potential (Supporting Information, Figure S4), while the neutral complex (^tBuN4)NiCl₂ 7 reveals a quasireversible oxidation wave at a more accessible potential of +0.52 V ($\Delta E_p = 125$ mV, Supporting Information, Figure S7),²⁸ assigned to a Ni^{II}/Ni^{III} one-electron oxidation based on coulometry measurements. Moreover, the bulk electrolysis of (^tBuN4)NiCl₂ in CH₂Cl₂ affords a brown product upon passing a charge corresponding to one electron through the electrolysis solution. The Ni(III) product is stable in the solid state, and its EPR spectrum reveals a pseudoaxial signal ($g_x = 2.194$, $g_y = 2.175$, $g_z = 2.023$) with superhyperfine coupling to two N-atoms ($A_z = 17$ G), consistent with the formation of a d⁷ Ni^{III} species with a d_{z²} ground state (Figure 6).

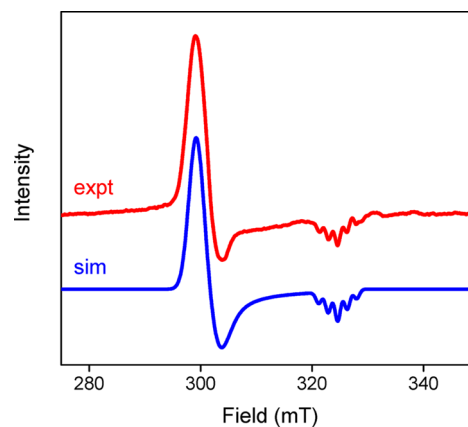


Figure 6. Experimental (red) and simulated (blue) EPR spectra of the product of electrolysis of the Ni(II) complex 7 (MeCN glass, 113 K).

Overall, these studies indicate that the ^tBuN4 ligand may be suitable to stabilize Co(I) and Ni(I), as well as the Fe(III) and Co(III) solvato-complexes, and also allow the formation of an isolable Ni(III) species obtained upon the oxidation of the neutral (^tBuN4)Ni^{II}Cl₂ complex. Current investigations are exploring the use of these complexes in multielectron redox transformations for energy-related applications.

Preliminary Reactivity Studies of (^tBuN4)M^{II} Complexes. The structural and electronic properties of the (^tBuN4)M^{II} complexes described herein reveal the redox flexibility of these systems, as well as their ability to interact with exogenous substrates because of the two available *cis* coordination sites. In this regard, we set out to begin exploring the reactivity of these complexes. The described reactivity of the Cu^{II} complex 4 and the Fe^{II} complex 1 highlight the

involvement of these complexes in both nonredox and redox processes. The full reactivity studies of these systems are currently underway and will be reported elsewhere.

(a). *Reactivity of $(^t\text{BuN4})\text{Cu}^{\text{II}}$ Complex toward Acetonitrile Hydrolytic Coupling.* By contrast to the formation of the bis-acetonitrile complex **4** under anhydrous conditions, the reaction of the hexahydrate precursor $\text{Cu}(\text{ClO}_4)_2 \cdot 6\text{H}_2\text{O}$ with 1 equiv of $^t\text{BuN4}$ in MeCN affords a dicationic N-acetylacetamidine complex **9** isolated in 56% yield that was characterized by X-ray diffraction (Figure 7, Scheme 1). The

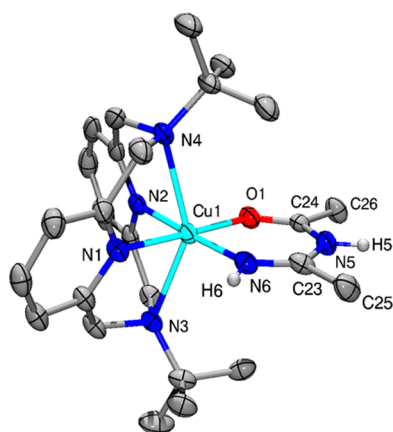
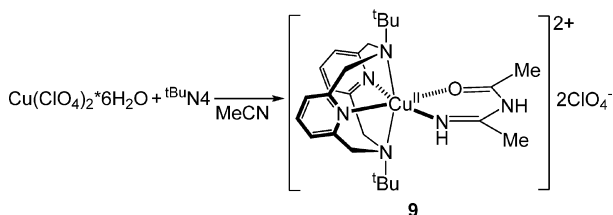


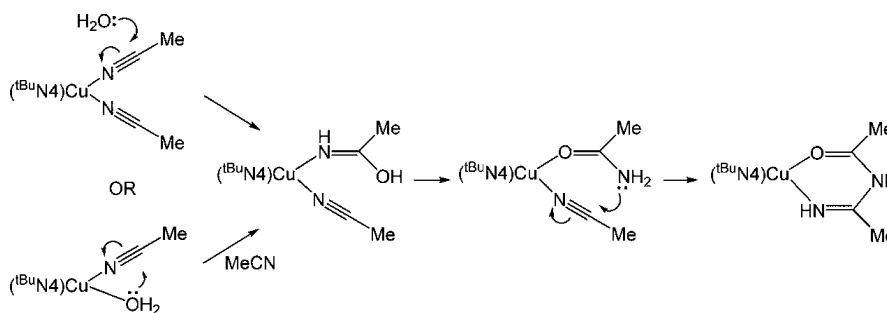
Figure 7. ORTEP plot (50% probability ellipsoids) for the cation of **9**. Selected bond distances (Å) and angles (deg): Cu(1)–O(1) 2.008(2); Cu(1)–N(6) 1.945(3); Cu(1)–N(1) 2.007(3); Cu(1)–N(2) 1.971(3); Cu(1)–N(3) 2.435(3); Cu(1)–N(4) 2.425(3); O(1)–C(24) 1.224(4); N(6)–C(23) 1.282(4); N(5)–C(23) 1.388(4); N(5)–C(24) 1.373(4); C(24)–N(5)–C(23) 128.5(3); O1–C24–C26 123.2(3); N6–C23–C25 124.9(3).

Scheme 1. Synthesis of the N-Acetylacetamidine Complex **9**



UV–vis spectrum reveals a broad d-d transition at 640 nm, and the Evans method measurements are consistent with the presence of a d^9 Cu^{II} center ($\mu_{\text{eff}} = 1.93 \mu_{\text{B}}$). The IR spectrum of **9** exhibits two absorptions at 3380 and 3250 cm^{-1} that are assigned as =NH and –NH stretching vibrations, respectively.³⁴

Scheme 2. Proposed Mechanism for the Formation of **9**



The presence of the two N–H groups of the N-acetylacetamidine ligand was confirmed by X-ray and is consistent with a dicationic complex and the presence of two perchlorate counteranions. While the C(23)–N(6) and C(24)–O(1) bond lengths of 1.282 Å and 1.224 Å in the N-acetylacetamidine ligand (Figure 7) are in the typical range for double C=N and C=O bonds, respectively, the N(5)–C distances are significantly longer (1.373–1.388 Å), indicative of a single bond character. The bond lengths of N-acetylacetamidine ligand in **9** are similar to the bond distances reported for the analogous N-acylamidine $\text{Cu}(\text{II})$ complexes.^{34,35} The chelating N-acetylacetamidine ring in **9** is essentially planar, including the N–H groups, while the O–C–C and N–C–C bond angles are 123.2° and 124.9°, respectively, consistent with the presence of sp^2 carbon atoms.

The observed hydrolytic coupling of two nitrile molecules to form a N-acylamidate chelate has only been reported for Ru complexes with aromatic nitriles³⁶ and Pt complexes with CCl_3CN , the latter system leading to further hydrolysis to diacetamide.³⁷ Similarly to the proposed mechanisms of hydrolytic coupling of nitriles in those complexes,^{36–38} the formation of **9** likely involves the initial hydrolysis of acetonitrile to acetamide followed by N(amide)-to-C(nitrile) coupling (Scheme 2). Such a facile nitrile hydrolysis in complex **9** suggests that a $(^t\text{BuN4})\text{Cu}^{\text{II}}$ center acts as a good Lewis acid, while coordination of two MeCN ligands in a *cis* orientation likely promotes their condensation. Importantly, to the best of our knowledge this is the first example of hydrolytic coupling of nitriles promoted by first row transition metal complexes. Moreover, there are only two other examples of N-acylamidine $\text{Cu}(\text{II})$ complexes previously reported in the literature that were synthesized by the direct reaction of $\text{Cu}(\text{II})$ precursors with N-acylamidines.^{34,35} Therefore, the observed reactivity is of appreciable interest for catalytic nitrile and amide hydrolysis using inexpensive Lewis acid catalysts.³⁸

(b). *Reactivity of $\text{Fe}(\text{II})$ Complex **1** with Oxidants.* The above results show that the $^t\text{BuN4}$ ligand can accommodate metal centers in various oxidation states. Since the oxidative reactivity of Fe^{II} complexes supported by multidentate N-donor ligands has been extensively investigated for the past decades, we began exploring the reactivity of the $[(^t\text{BuN4})\text{Fe}^{\text{II}}(\text{MeCN})_2]^{2+}$ complex **1** with various oxidants. In the initial studies, PhIO was added in 1 equiv aliquots to a solution of **1** in MeCN at -35°C . The UV–vis spectrum shows a gradual disappearance of the starting material; however no intermediates were observed. After addition of 5 equiv of PhIO, ~50% of **1** disappeared, and warming up the solution to RT completed the decomposition of **1** to give a pale yellow solution.

The reactivity of **1** with H_2O_2 in MeCN leads to the disappearance of the starting material at $-35\text{ }^\circ\text{C}$, and no intermediates were observed under these conditions. However, when **1** was dissolved in MeOH containing 5 equiv of Et_3N and reacted with 10 equiv of H_2O_2 at $-70\text{ }^\circ\text{C}$, formation of a transient species that exhibits a weak absorption band at 780 nm was observed 2–3 min after addition of H_2O_2 , followed by its decay after 40 min at $-70\text{ }^\circ\text{C}$ (Figure 8).

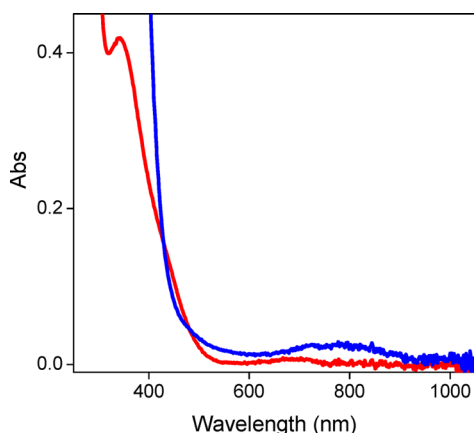


Figure 8. Reaction of **1** with 10 equiv of H_2O_2 in the presence of 10 equiv of Et_3N in MeOH at $-70\text{ }^\circ\text{C}$ ($[\mathbf{1}] = 1.1\text{ mM}$; 10 mm path length): (a) UV-vis spectrum of **1** (red); (b) UV-vis spectrum 3 min after addition of H_2O_2 at $-70\text{ }^\circ\text{C}$ (blue).

The Fe(II) species that reacts with H_2O_2 under the above conditions is likely a Fe(II)-methoxo complex, as the characteristic visible band at 669 nm of the starting bis-acetonitrile complex **1** disappears upon addition of Et_3N . A large scale oxidation of **1** in MeOH in the presence of 5 equiv of Et_3N and 10 equiv of H_2O_2 allowed the isolation of complex $[(^t\text{BuN}4)\text{Fe}^{\text{III}}(\text{OMe})_2](\text{OTf})$, **10**, in 80% yield that was characterized by X-ray diffraction (Figure 9). The X-ray structure of **10** reveals a distorted octahedral geometry with

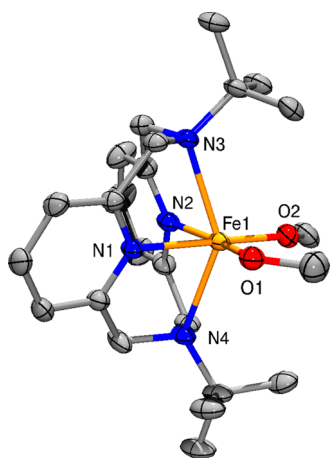


Figure 9. ORTEP plot (50% probability ellipsoids) for the cation of **10**. Selected bond distances (Å) and angles (deg): Fe(1)–N(1) 2.114(2); Fe(1)–N(2) 2.134(2); Fe(1)–N(3) 2.318(2); Fe(1)–N(4) 2.352(2); Fe(1)–O(2) 1.861(2); Fe(1)–O(1) 1.868(2); N(1)–Fe(1)–N(2) 81.02(9), N(3)–Fe(1)–N(4) 140.08(8). The angles between the plane of pyridine rings and mean equatorial plane are 74.84° and 75.88° .

average Fe– N_{py} and Fe– N_{am} distances of 2.124 and 2.335 Å, respectively, 0.17–0.22 Å longer than in **1**. As expected, the $^t\text{BuN}4$ ligand is significantly twisted in **10**, with angles between the average pyridine ring planes and a mean equatorial plane of 74.84° and 75.88° . The Evans method measurements of **10** in MeOH give a μ_{eff} of $1.61\ \mu_{\text{B}}$, supporting a low spin Fe(III) center (the μ_{eff} value is lower than the spin-only value likely because of a partial dimerization in solution).³⁹

The intermediate formed upon addition of H_2O_2 exhibits a weak absorption band at 780 nm that is reminiscent of characteristic near-IR bands observed for low spin Fe(IV)-oxo complexes obtained through oxidation of Fe(II) precursors with peroxides, PhIO, or peracetic acid.^{40–43} For example, Fe(IV)-oxo complexes supported by a tetradentate pyridyl/amine TMPA ligand, $[(\text{TMPA})\text{Fe}^{\text{IV}}(\text{O})\text{X}]^{2+/+}$ (X = MeCN, OTf, Br, Cl) exhibit absorption bands at 724–800 nm.⁴¹ The absence of such intermediate in detectable concentrations upon oxidation of **1** with PhIO or H_2O_2 in MeCN could be due to lower stability of this species at higher temperatures ($-35\text{ }^\circ\text{C}$). The formation of a Fe(III)-hydroperoxo or -peroxo species by reaction with excess H_2O_2 under these conditions can be ruled out as the addition of excess H_2O_2 after complete decay of the transient intermediate does not lead to the reappearance of a 780 nm band. Similarly, the isolated Fe(III) product from the reaction with H_2O_2 does not react with excess $\text{H}_2\text{O}_2/\text{Et}_3\text{N}$ under analogous conditions. In addition, the fast decay of the observed intermediate at $-70\text{ }^\circ\text{C}$ implies that the Fe(IV)-oxo species supported by $^t\text{BuN}4$ is significantly less stable compared to analogous species supported by other tetradentate N-donor ligands such as TMPA or TMC (TMC = 1,4,8,11-tetramethyl-1,4,8,11-tetraazacyclotetradecane).^{41,44} Overall, the formation of a high-valent Fe intermediate suggests that $^t\text{BuN}4$ should be able to promote oxidation reactivity toward exogenous substrates, especially given its coordination arrangement that enforces two available *cis* coordination sites.⁴⁵ Detailed studies are currently underway to unambiguously identify the transient species, and they will be reported elsewhere.

The reaction of **1** in MeCN solution with 4 equiv of peracetic acid at $-35\text{ }^\circ\text{C}$ leads to the fast formation of a purple species characterized by an absorption band at 535 nm and a broad weaker band at $\sim 850\text{ nm}$ (Figure 10); this species decays at $-35\text{ }^\circ\text{C}$ within 20–30 min to give a clear yellow solution. Notably, formation of this intermediate requires more than 1 equiv of peracetic acid, suggesting that an initial formation of an Fe(III) species may be needed before generation of the purple species. Attempts to crystallize the product of the reaction of **1** with 1 equiv of peracetic acid were not successful, yet it is likely a Fe(III) complex with acetate (and acetonitrile) ligands, as suggested by the observed IR characteristic stretches^{46,47} and by analogy to the reactivity of other Fe(II) complexes supported by N-donor polydentate ligands.⁴¹

The formation of the purple intermediate species upon addition of excess peracetic acid is intriguing, and we are currently investigating this reactivity in detail. For example, we have investigated this intermediate by EPR under the conditions of the UV-vis experiment. Complex **1** was reacted with 4 equiv of peracetic acid in MeCN at $-35\text{ }^\circ\text{C}$, and the generated solution was frozen in liquid N_2 after 5 min. The EPR spectrum reveals a broad rhombic signal indicative of an $S = 1/2$ system that was simulated using the following parameters: $g_x = 2.153$; $g_y = 2.105$, $g_z = 1.957$ (Figure 11); this intermediate species decays even at low temperature to generate high-spin Fe(III) product(s) (Supporting Information,

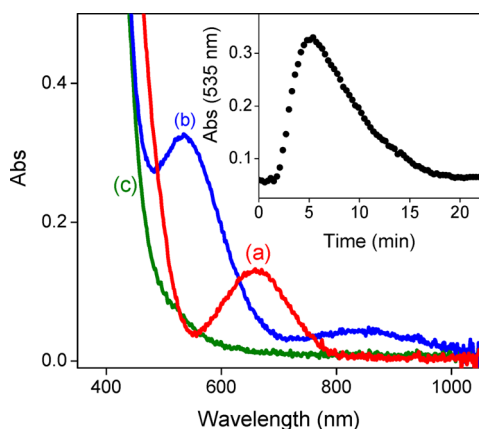


Figure 10. Reaction of **1** with 4 equiv of peracetic acid in MeCN at $-35\text{ }^{\circ}\text{C}$ ($[\mathbf{1}] = 1.1\text{ mM}$; 10 mm path length): (a) UV-vis spectrum of **1** before reaction (red); (b) UV-vis spectrum 5 min after addition of 4 equiv of peracetic acid at $-35\text{ }^{\circ}\text{C}$ (blue); (c) UV-vis spectrum 20 min after addition of 4 equiv of peracetic acid at $-35\text{ }^{\circ}\text{C}$ (green); inset: formation and disappearance of the intermediate followed by changes in the absorbance at 535 nm.

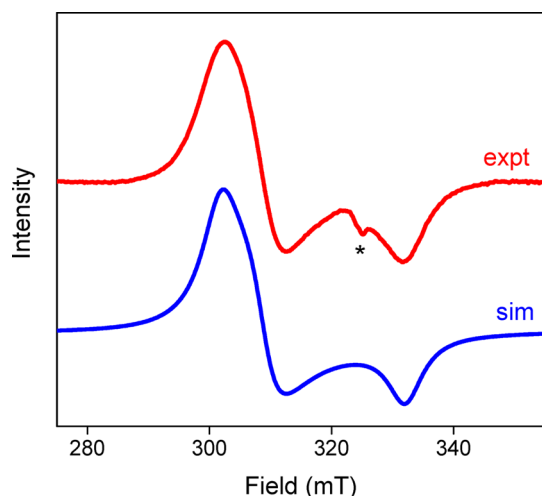


Figure 11. Experimental (red) and simulated (blue) EPR spectra of the product of reaction of **1** with 4 equiv of peracetic acid in MeCN after 5 min at $-35\text{ }^{\circ}\text{C}$ (MeCN glass at 77 K). Simulated spectrum parameters: $g_x = 2.153$; $g_y = 2.105$; $g_z = 1.957$. The signal marked with an asterisk at $g = 2.00$ is likely due to an organic radical impurity.

Figure S22).²⁸ On the basis of these preliminary observations, we tentatively assigned this unstable intermediate species to either a low-spin Fe(V)-oxo intermediate or a low-spin Fe(III)-acetylperoxo species (Scheme 3), both of which could

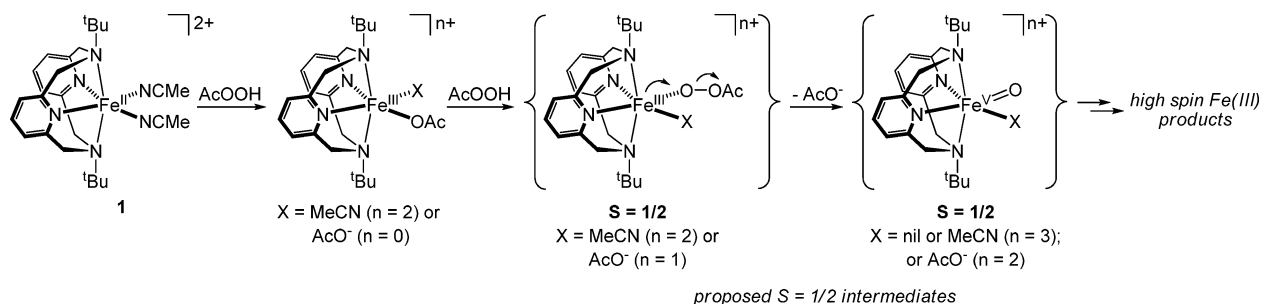
give rise to the observed rhombic EPR signal.^{48–50} Such low-spin Fe(V) or Fe(III) species have been detected spectroscopically only in very few cases. For example, the detection of Fe(V)-oxo species formed via the oxidation of Fe(III) precursors with meta-chloroperoxybenzoic acid (mCPBA), H_2O_2 , or oxone was reported recently.^{45,48,49,51–53} Importantly, such intermediates were proposed to play a role in catalytic oxidation reactions: a similar Fe(V)-oxo species was proposed based on ESI-MS studies as an intermediate during the *cis*-hydroxylation of alkenes catalyzed by the $(^{\text{Me}}\text{N}4)\text{Fe}(\text{III})$ complex.⁴⁵ In addition, formation of an Fe(III)-acetylperoxo was suggested based on EPR for a nonheme Fe complex during the oxidation of $(\text{TPA})\text{Fe}^{\text{II}}(\text{MeCN})_2^{2+}$ with excess mCPBA.⁵⁰ Overall, although the transient intermediate observed during the oxidation of **1** cannot be conclusively assigned as either an oxoiron(V) or an acylperoxoiron(III) species at this stage, more detailed studies are directed toward characterization of this species and its reactivity in catalytic oxidation reactions.

CONCLUSION

Described herein is the synthesis of a number of cationic solvato-complexes of late first-row transition metal ions (Fe^{II} , Co^{II} , Ni^{II} , Cu^{II} , Cu^{I} , Zn^{II}) supported by the macrocyclic ligand *N,N'*-di-*tert*-butyl-2,11-diaza[3.3](2,6)pyridinophane ($^{\text{tBu}}\text{N}4$). In these complexes, $^{\text{tBu}}\text{N}4$ acts as a tetradentate ligand leaving two *cis* coordination sites to be occupied by a solvent (MeCN) or a counteranion. The bis-acetonitrile complexes are prone to lose the coordinated solvent under vacuum. In all $(^{\text{tBu}}\text{N}4)\text{M}$ complexes described herein, the axial metal– N_{amine} distances are significantly longer than the equatorial $\text{M}–\text{N}_{\text{py}}$ distances, and the overall geometry can be described as distorted octahedral for the complexes of Fe^{II} , Co^{II} , Ni^{II} , Cu^{II} , and Zn^{II} . The study of the magnetic properties of $[(^{\text{tBu}}\text{N}4)\text{M}(\text{MeCN})_2](\text{OTf})_2$ ($\text{M} = \text{Fe}, \text{Co}$) and comparison with analogous reported complexes suggest that these complexes exhibit μ_{eff} values and magnetic properties that are intermediate between those expected for high spin and low spin complexes. Electrochemical studies reveal that $^{\text{tBu}}\text{N}4$ is suitable to stabilize Co^{I} and Ni^{I} , as well as Fe^{III} and Co^{III} complexes, while the electrochemical oxidation of $(^{\text{tBu}}\text{N}4)\text{NiCl}_2$ generates an isolable Ni^{III} complex that was characterized by EPR.

Initial reactivity studies have been performed to highlight the potentially rich chemistry of these complexes. The $(^{\text{tBu}}\text{N}4)\text{Cu}^{\text{II}}$ complex acts as a good Lewis acid and promotes a rarely observed hydrolytic coupling of two MeCN molecules to produce a Cu^{II} complex with a coordinated *N*-acetylacetamide ligand. The reaction of $[(^{\text{tBu}}\text{N}4)\text{Fe}^{\text{II}}(\text{MeCN})_2](\text{OTf})_2$ with H_2O_2 in the presence of Et_3N in MeOH likely leads to the formation of an unstable high-valent Fe species detected by

Scheme 3. Proposed Formation of $S = 1/2$ Intermediate(s) during the Reaction of **1** with Excess Peracetic Acid



UV-vis and eventually to the formation of the $[(^t\text{Bu}_4\text{N})\text{Fe}^{\text{III}}(\text{OMe})_2](\text{OTf})$ product. Interestingly, a transient intermediate was also detected by UV-vis upon the oxidation of $[(^t\text{Bu}_4\text{N})\text{Fe}^{\text{II}}(\text{MeCN})_2](\text{OTf})_2$ with excess peracetic acid, and EPR suggests the formation of a low-spin $S = 1/2$ intermediate tentatively assigned to an $\text{Fe}^{\text{V}}\text{-oxo}$ or an $\text{Fe}^{\text{III}}\text{-acetylperoxo}$ species, although current detailed studies are needed to confirm the identity of the observed intermediate. Overall, the results described herein establish that $^t\text{N}_4$ ligands are an appropriate platform for stabilizing late first row transition metal ions in various oxidation states and thus should be able to promote multielectron redox transformations.^{7–10} Such complexes are currently being evaluated for their ability to activate small molecules such as O_2 , H_2 , CO_2 , and H_2O , as well as for catalytic oxidation reactions.

■ ASSOCIATED CONTENT

■ Supporting Information

Crystallographic data in CIF format. Further details are given in Figures S1–S35 and Tables S1–S28. This material is available free of charge via the Internet at <http://pubs.acs.org>.

■ AUTHOR INFORMATION

Corresponding Author

*E-mail: mirica@wustl.edu.

Notes

The authors declare no competing financial interest.

■ ACKNOWLEDGMENTS

We thank Washington University for startup funds and the DOE Catalysis Science Program (DE-FG02-11ER16254) for support. L.M.M. is a Sloan Fellow.

■ REFERENCES

- (1) Bertini, I.; Gray, H. B.; Steifel, E. I.; Valentine, J. S. *Biological Inorganic Chemistry: Structure and Reactivity*; University Science Books: Sausalito, CA, 2006.
- (2) Kraatz, H. B.; Metzler-Nolte, N. *Concepts and Models in Bioinorganic Chemistry*; Wiley-VCH: Weinheim, Germany, 2006.
- (3) Holm, R. H.; Solomon, E. I. *Chem. Rev.* **2004**, *104*, 347–348, and other reviews in the same issue.
- (4) Costas, M.; Mehn, M. P.; Jensen, M. P.; Que, L., Jr. *Chem. Rev.* **2004**, *104*, 939–986.
- (5) Che, C. M.; Li, Z. Y.; Wong, K. Y.; Poon, C. K.; Mak, T. C. W.; Peng, S. M. *Polyhedron* **1994**, *13*, 771–776.
- (6) Meneghetti, S. P.; Lutz, P. J.; Fischer, J.; Kress, J. *Polyhedron* **2001**, *20*, 2705–2710.
- (7) Khusnutdinova, J. R.; Rath, N. P.; Mirica, L. M. *J. Am. Chem. Soc.* **2010**, *132*, 7303–7305.
- (8) Khusnutdinova, J. R.; Rath, N. P.; Mirica, L. M. *J. Am. Chem. Soc.* **2012**, *134*, 2414–2422.
- (9) Tang, F.; Zhang, Y.; Rath, N. P.; Mirica, L. M. *Organometallics* **2012**, *31*, 6690–6696.
- (10) Tang, F.; Qu, F.; Khusnutdinova, J. R.; Rath, N. P.; Mirica, L. M. *Dalton Trans.* **2012**, *41*, 14046–14050.
- (11) Mirica, L. M.; Khusnutdinova, J. R. *Coord. Chem. Rev.* **2013**, *299*–314.
- (12) Koch, W. O.; Krüger, H.-J. *Angew. Chem., Int. Ed.* **1995**, *34*, 2671–2674.
- (13) Kelm, H.; Krüger, H.-J. *Inorg. Chem.* **1996**, *35*, 3533–3540.
- (14) Koch, W. O.; Schünemann, V.; Gerdan, M.; Trautwein, A. X.; Krüger, H.-J. *Chem.—Eur. J.* **1998**, *4*, 686–691.
- (15) Graf, M.; Wolmershäuser, G.; Kelm, H.; Demeschko, S.; Meyer, F.; Krüger, H.-J. *Angew. Chem., Int. Ed.* **2010**, *49*, 950–953.

- (16) Kubas, G. J.; Monzyk, B.; Crumbliss, A. L. *Inorg. Synth.* **1979**, *19*, 90–92.
- (17) Evans, D. F. *J. Chem. Soc.* **1959**, 2003–2005.
- (18) De Buysser, K.; Herman, G. G.; Bruneel, E.; Hoste, S.; Van Driessche, I. *Chem. Phys.* **2005**, *315*, 286–292.
- (19) *Apex II, SAINT, SADABS*; Bruker Analytical X-ray: Madison, WI, 2010.
- (20) Sheldrick, G. *Acta Crystallogr. Sect. A: Found. Crystallogr.* **2008**, *64*, 112–122.
- (21) Krüger, H.-J. *Chem. Ber.* **1995**, *128*, 531–539.
- (22) Gülich, P.; Goodwin, H. A. *Spin Crossover in Transition Metal Compounds II*; Springer: Berlin, Germany, 2004.
- (23) Addison, A. W.; Rao, T. N.; Reedijk, J.; van Rijn, J.; Verschoor, G. C. *J. Chem. Soc., Dalton Trans.* **1984**, 1349–1356.
- (24) Cotton, F. A.; Wilkinson, G. *Advanced Inorganic Chemistry*, 5th ed.; Wiley-Interscience: New York, 1988.
- (25) Day, M. C.; Selbin, J. *Theoretical inorganic chemistry*; Reinhold Book Corp.: New York, 1969.
- (26) Krivokapic, I.; Zerara, M.; Daku, M. L.; Vargas, A.; Enachescu, C.; Ambrus, C.; Tregenna-Piggott, P.; Amstutz, N.; Krausz, E.; Hauser, A. *Coord. Chem. Rev.* **2007**, *251*, 364–378.
- (27) Lever, A. D. P. *Inorganic Electronic Spectroscopy*, 2nd ed.; Elsevier: Amsterdam, The Netherlands, 1984.
- (28) See Supporting Information.
- (29) Geiger, W. E. In *Progress in Inorganic Chemistry*; John Wiley & Sons, Inc.: New York, 1985; pp 275–352.
- (30) Zanello, P. *Inorganic Electrochemistry. Theory, Practice and Application*; RSC: Cambridge, U.K., 2003.
- (31) Börzel, H.; Comba, P.; Hagen, K. S.; Katsichtis, C.; Pritzkow, H. *Chem.—Eur. J.* **2000**, *6*, 914–919.
- (32) Lee, D.-H.; Murthy, N. N.; Karlin, K. D. *Inorg. Chem.* **1997**, *36*, 5785–5792.
- (33) Bigi, J. P.; Hanna, T. E.; Harman, W. H.; Chang, A.; Chang, C. J. *Chem. Commun.* **2010**, *46*, 958–960.
- (34) Eberhardt, J. K.; Fröhlich, R.; Venne-Dunker, S.; Würthwein, E.-U. *Eur. J. Inorg. Chem.* **2000**, *2000*, 1739–1743.
- (35) Eberhardt, J. K.; Glaser, T.; Hoffmann, R.-D.; Fröhlich, R.; Würthwein, E.-U. *Eur. J. Inorg. Chem.* **2005**, *2005*, 1175–1181.
- (36) Hiraki, K.; Kinoshita, Y.; Kinoshita-Kawashima, J.; Kawano, H. *J. Chem. Soc., Dalton Trans.* **1996**, 291–298.
- (37) Rochon, F. D.; Kong, P. C.; Melanson, R. *Inorg. Chem.* **1990**, *29*, 2708–2712.
- (38) Kukushkin, V. Y.; Pombeiro, A. J. L. *Inorg. Chim. Acta* **2005**, *358*, 1–21.
- (39) Klein Gebbink, R. J. M.; Jonas, R. T.; Goldsmith, C. R.; Stack, T. D. P. *Inorg. Chem.* **2002**, *41*, 4633–4641.
- (40) Kaizer, J.; Klinker, E. J.; Oh, N. Y.; Rohde, J.-U.; Song, W. J.; Stubna, A.; Kim, J.; Münck, E.; Nam, W.; Que, L. *J. Am. Chem. Soc.* **2004**, *126*, 472–473.
- (41) Rohde, J.-U.; Stubna, A.; Bominaar, E. L.; Münck, E.; Nam, W.; Que, L. *Inorg. Chem.* **2006**, *45*, 6435–6445.
- (42) Nam, W. *Acc. Chem. Res.* **2007**, *40*, 522–531.
- (43) Krebs, C.; Galonić Fujimori, D.; Walsh, C. T.; Bollinger, J. M. *Acc. Chem. Res.* **2007**, *40*, 484–492.
- (44) Rohde, J.-U.; In, J.-H.; Lim, M. H.; Brennessel, W. W.; Bukowski, M. R.; Stubna, A.; Münck, E.; Nam, W.; Que, L., Jr. *Science* **2003**, *299*, 1037–1039.
- (45) Chow, T. W.-S.; Wong, E. L.-M.; Guo, Z.; Liu, Y.; Huang, J.-S.; Che, C.-M. *J. Am. Chem. Soc.* **2010**, *132*, 13229–13239.
- (46) Smith, J. M.; Long, J. R. *Inorg. Chem.* **2010**, *49*, 11223–11230.
- (47) Fernandes, C.; Stadler, E.; Drago, V.; Jorge da Cunha, C.; Hiroko Kuwabara, I. *Spectrochim. Acta, Part A* **1996**, *52*, 1815–1821.
- (48) de Oliveira, F. T.; Chanda, A.; Banerjee, D.; Shan, X.; Mondal, S.; Que, L.; Bominaar, E. L.; Münck, E.; Collins, T. J. *Science* **2007**, *315*, 835–838.
- (49) Lyakin, O. Y.; Bryliakov, K. P.; Talsi, E. P. *Inorg. Chem.* **2011**, *50*, 5526–5538.
- (50) Guisado-Barrios, G.; Zhang, Y.; Harkins, A. M.; Richens, D. T. *Inorg. Chem. Commun.* **2012**, *20*, 81–85.

(51) Lyakin, O. Y.; Bryliakov, K. P.; Britovsek, G. J. P.; Talsi, E. P. *J. Am. Chem. Soc.* **2009**, *131*, 10798–10799.

(52) Prat, I.; Mathieson, J. S.; Güell, M.; Ribas, X.; Luis, J. M.; Cronin, L.; Costas, M. *Nat. Chem.* **2011**, *3*, 788–793.

(53) Van Heuvelen, K. M.; Fiedler, A. T.; Shan, X.; De Hont, R. F.; Meier, K. K.; Bominaar, E. L.; Münck, E.; Que, L. *Proc. Natl. Acad. Sci. U.S.A.* **2012**, *109*, 11933–11938.